Materials Science & Engineering A 707 (2017) 708–716

Contents lists available at ScienceDirect

Materials Science & Engineering A

journal homepage: www.elsevier.com/locate/msea

Microstructure and mechanical behaviors of $Gd_xCoCrCuFeNi$ high-entropy alloys

L.J. Zhang[a], P.F. Yu[a], M.D. Zhang[a], D.J. Liu[a], Z. Zhou[a], M.Z. Ma[a], P.K. Liaw[b], G. Li[a,b,*], R.P. Liu[a]

[a] State Key Laboratory of Metastable Materials Science and Technology, Yanshan University, Qinhuangdao 066004, China
[b] Department of Materials Science and Engineering, The University of Tennessee, Knoxville, TN 37996, USA

ARTICLE INFO

Keywords:
High-entropy alloys
Rare earth element
Microstructure
Mechanical properties

ABSTRACT

A new series of $Gd_xCoCrCuFeNi$ (x = 0, 0.05, 0.1, 0.2, and 0.3) high entropy alloys were synthesized to investigate alloying effects of the rare-earth element, Gd, on the microstructure and mechanical behaviors. Microstructures of these alloys were examined using X-ray diffraction, scanning electron microscopy, and transmission electron microscopy, and the phase evolution was characterized and compared using the previous criteria. It was found that the microstructure changes from the face-centered cubic matrix plus Cu-rich face-centered cubic phase to face-centered cubic matrix plus hexagonal structure phase ($CaCu_5$ type) with the addition of Gd. The volume fraction of the hexagonal structure phase increases with increasing the Gd content, which is mainly responsible for the increment in the Vickers hardness, yield and fracture strength. Nanoindentation measurements show that the hexagonal structure phase is harder. Furthermore, the dislocation nucleation of the face-centered cubic and hexagonal structure phases was probed by measuring the first pop-in behavior in the load-displacement curve. With the increase of Gd, the series of $Gd_xCoCrCuFeNi$ high entropy alloys show different fracture and strengthening mechanisms. The close relationship between the structure and strength of the series alloys are discussed.

1. Introduction

Recently, high-entropy alloys (HEAs), which are defined as solid solution alloys that contain more than four principal elements in equal or near equal atomic percent (at%), have attracted increasing attentions in materials science and engineering [1–9]. The new alloy-design concept has challenged the proposed theories, models, and methods for conventional alloys, which contain one and rarely two base elements. Many excellent properties are associated with the four core effects for HEAs summarized by Yeh [1]: high-entropy effects, sluggish diffusion, severe lattice distortion, and cocktail effects. A large number of novel properties of HEAs have been founded, such as their superb specific strength [2], good fatigue [3,4], fracture resistance at cryogenic temperatures [5], high magnetic saturation [6], oxidation, and corrosion resistance [7,8], and radiation tolerance [9]. Because of their considerable structural and functional potential as well as richness of design, HEAs are promising candidates for practical applications and further researches.

In the previous studies, the modification of the chemical compositions of the HEAs has become the effective approach to control the phase selection and the formation of precipitation to attain excellent properties [10–18]. For example, the single phase face-centered cubic (FCC) CoCrFeNi and CoCrFeMnNi HEAs have been effectively strengthened by the addition of Al element because of the formation of the hard body-centered cubic (BCC) phase [10,11]. By the addition of Mo, the $CoCrFeNiMo_{0.3}$ HEA was tremendously strengthened by the precipitation of hard σ and μ intermetallic compounds with a tensile strength as high as 1.2 GPa and a good ductility of ~ 19% [12]. The additions of other alloying elements, such as V [13], Nb [14], Fe [15], Ti [15,16], Si [17], and Zr [18], were investigated to improve the microstructures and mechanical properties of different kinds of HEA systems. Rare-earth elements as important additives can improve many properties of the aluminum alloy and magnesium alloy, such as strength, heat resistance, creep resistance, extrusion behavior and so on [19–22]. The maximum tensile strength and best comprehensive performance of the AZ80 magnesium alloy can be achieved by adding a rare-earth element Gd [22]. However, there are few reports about the effect of rare-earth element on the microstructure and properties of HEAs. In the present work, the CoCrCuFeNi alloy was selected as the base alloy and the rare-earth element, Gd, was chosen as the alloying element based on the following reasons. Firstly, the addition of Cu cannot improve the mechanical properties of the alloy because the Cu

* Corresponding author. at: State Key Laboratory of Metastable Materials Science and Technology, Yanshan University, Qinhuangdao 066004, China.
E-mail addresses: gli25@utk.edu, gongli@ysu.edu.cn (G. Li), riping@ysu.edu.cn (R.P. Liu).

http://dx.doi.org/10.1016/j.msea.2017.09.102
Received 26 July 2017; Received in revised form 11 August 2017; Accepted 21 September 2017
Available online 22 September 2017
0921-5093/

has the positive mixing enthalpy with other elements of the alloy and the segregation of Cu makes the formation of the soft FCC phase around grain boundary to make the alloy possesses an excellent plasticity but low strength. Secondly, the rare-earth element, Gd, is the HCP structure stabilizer. Because of the low negative mixing enthalpy with the elements of Cu, Ni, and Co, the formation of the stable binary or ternary hexagonal structure composition [23,24] may be the dominant hardening factor of CoCrCuFeNi alloy. What is more, the alloying rare-earth element, Gd, and the constituent elements of CoCrCuFeNi alloy have low negative mixing enthalpy and high radius difference. It is important and interesting to get better understanding of the phase selection mechanism and the fracture and strengthening mechanisms of the $Gd_xCoCrCuFeNi$ HEAs. The characterization of the structure evolution and mechanical properties of $Gd_xCoCrCuFeNi$ HEAs can provide some new clues to the design of new HEA system with excellent properties.

2. Experimental

Alloy ingots of $Gd_xCoCrCuFeNi$ (x = 0, 0.05, 0.1, 0.2, and 0.3) were synthesized in a vacuum arc melting furnace with a water-cooled Cu crucible under a Ti-gettered high-purity argon atmosphere by arc-melting a mixture of pure metals (purity > 99 wt%). These ingots were remelted at least five times to ensure chemical homogeneity. These alloys were denoted as Gd_0, $Gd_{0.05}$, $Gd_{0.1}$, $Gd_{0.2}$, and $Gd_{0.3}$, respectively. The crystal structure were identified by X-ray diffraction (XRD) with the Cu-Ka radiation scanning from 20° to 100° at a scanning speed of 4°/min. The microstructures of the as-cast specimens and the fracture surface morphology were characterized by scanning electron microscope (SEM, Hitachi S-4800), and the chemical compositions were analyzed by the SEM energy-dispersive spectrometry (EDS). The microstructure after compression was confirmed through transmission electron microscopy (TEM) observations which were performed at 200 kV in a JEM-2010 microscope equipped with selected area electron diffraction (SAED). Vickers hardness measurements were conducted, using a hardness tester (HVS-1000) under a load of 500 g for 10 s, and for each specimen, at least 10 measurements were carried out to obtain an average value. Room-temperature compression tests were performed, using an Instron 5982 machine under a strain rate of 5×10^{-4} s^{-1}. In this test, we employed at least two cylindrical specimens 3 mm in diameter and 6 mm in length for each alloy.

The nanoindentation experiments were performed at room temperature, using a Hysitron Triboindenter (TI-900) equipped with the in-situ atomic force microscope (AFM), and with a Berkovich diamond tip where the effective tip radius was about 450 nm. All of the samples must be polished to a mirror of 10 nm. The two different phases can be identified through the optical microscope equipped on the Triboindenter. The alloys were uploaded to the maximum load of 5000 μN at the loading rate of 1000 μN s^{-1} with a fixed holding time of 2 s, followed by reducing to zero to measure the nanohardness and elastic modulus on different phases. The incipient plasticity was probed by measuring the first pop-in behavior in the loading segment of the load-displacement (*P-h*) curve under a constant loading rate of 50 μN s^{-1} to 1000 μN. Thermal drift was maintained below 0.05 nm/s in all experiments.

3. Results

3.1. Crystal structure and microstructures

The XRD patterns from the as-cast $Gd_xCoCrCuFeNi$ alloys are shown in Fig. 1. The result indicates that all this series of alloys have a solid-solution matrix phase with an FCC crystal structure. However, for the Gd_0 and $Gd_{0.05}$ alloys, a minor reflection peak close to the right of the matrix appeared as shown in Fig. 1. The minor reflection peak was identified as a Cu-rich FCC phase. With increasing the Gd content, the reflection peaks corresponding to the hexagonal-structure (HS) phase

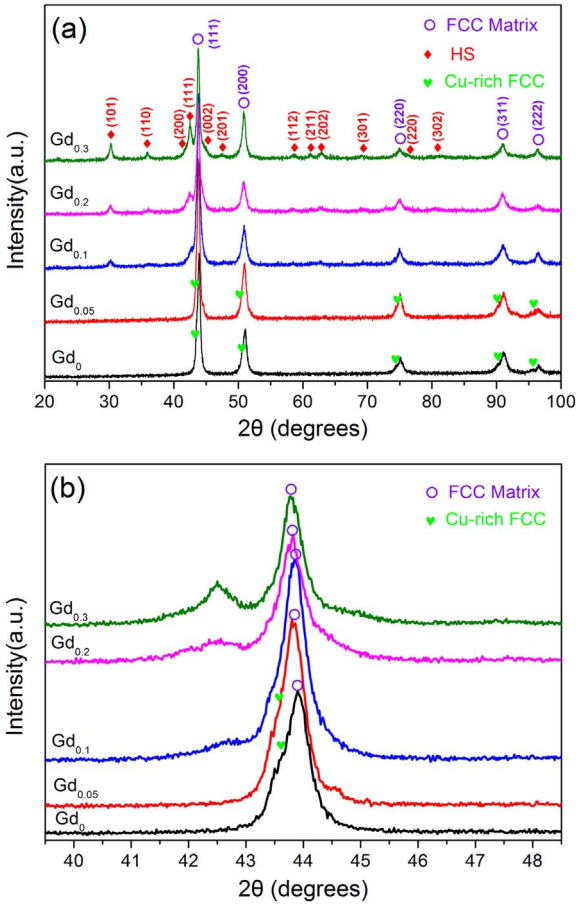

Fig. 1. (a) XRD patterns of the as-cast $Gd_xCoCrCuFeNi$ (x = 0, 0.05, 0.1, 0.2, and 0.3) alloys and (b) the detailed scans for the (111) peak of the FCC matrix phase.

can be obviously observed in the $Gd_{0.1}$, $Gd_{0.2}$, and Gd_{03} alloys. The HS phase can be identified as Gd (Cu, Co, Cr, Fe, Ni)$_5$ with the space group *P6/mmm* ($CaCu_5$ type) and the lattice parameters: a = 5.0023 Å and c = 4.0293 Å. With the Gd concentration increasing from 0.1 to 0.3, the relative intensity of the FCC solid-solution matrix diffraction peaks reduces while the HS phase diffraction peaks enhance, indicating that the volume fraction of the HS phase increases with the increment of the Gd concentration. Moreover, the detailed scans for the (111) peak of the FCC matrix phase are also shown in Fig. 1(b). It is noticed that this peak shifts towards a lower 2θ angle when the Gd concentration increases. This trend is identical to the variation of the lattice parameters of the FCC matrix phase, which are estimated to be 2.9114, 2.9166, 2.9172, 2.9198, and 2.9205 Å from the strongest (110) FCC peak of the Gd_0, $Gd_{0.05}$, $Gd_{0.1}$, $Gd_{0.2}$, and Gd_{03} alloys. In addition, the lattice-parameter difference of the FCC matrix phase as a function of the Gd content was depicted in Fig. 2. The lattice-parameter difference can be expressed as $(|a\text{-}a_0|)/a_0$, where a_0 is the lattice parameter of the FCC matrix in the CoCrCuFeNi alloy. The results show that the lattice-parameter difference increases with the increase of the Gd content. It is confirmed that rare-earth element, Gd, with a large atomic radius than other constituent elements (see Table 2), can be partly dissolved into the FCC matrix phase of the CoCrCuFeNi HEA and result in an increase of the lattice parameters.

Microstructures of the as-cast alloys with different Gd contents were displayed in Fig. 3. The structures of the five alloys were identified as dendrite (DR) and interdendrite (ID) structures. The DR structure of each alloy with different Gd contents is the Cu-depleted phase, which is the FCC matrix phase with a high volume fraction shown in Fig. 3(f). However, the ID structures are the Cu-rich phases which have different crystal structures with different Gd contents. For the Gd_0 and $Gd_{0.05}$

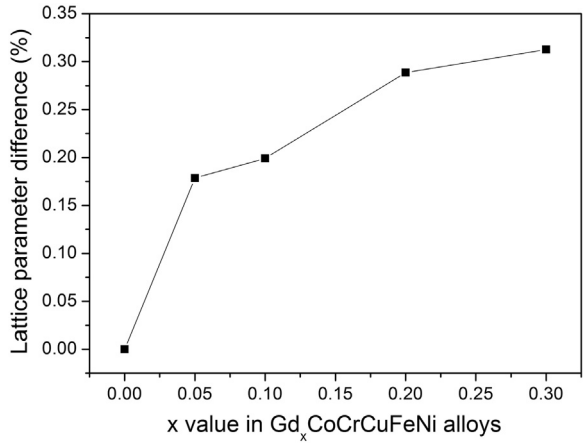

Fig. 2. Lattice parameter difference of the FCC matrix as a function of the Gd content in the as-cast $Gd_xCoCrCuFeNi$ (x = 0, 0.05, 0.1, 0.2, and 0.3) alloys.

Table 1
Chemical compositions and crystal structures of different regions in the $Gd_xCoCrCuFeNi$ high-entropy alloys by EDS (at%).

Alloys	Regions	Crystal structure	Chemical compositions (at%)					
			Cr	Fe	Co	Ni	Cu	Gd
Gd_0	DR	FCC	23.30	23.03	23.91	20.14	9.61	0
	ID	FCC (Cu-rich)	8.59	9.59	9.88	10.46	61.48	0
$Gd_{0.05}$	DR	FCC	23.46	23.20	23.47	20.15	9.71	0.01
	ID	FCC (Cu-rich)	11.36	10.20	10.11	12.01	56.11	0.21
$Gd_{0.1}$	DR	FCC	24.71	24.28	24.41	19.59	6.88	0.13
	ID	HS	7.46	7.66	7.49	14.53	59.57	3.28
$Gd_{0.2}$	DR	FCC	27.34	25.34	24.71	17.11	5.14	0.36
	ID	HS	8.94	9.31	10.38	23.01	37.89	10.48
$Gd_{0.3}$	DR	FCC	27.83	26.01	25.46	16.37	3.76	0.57
	ID	HS	2.21	3.97	6.99	25.11	45.32	16.04

Table 2
Mixing enthalpy of different atom pairs, ΔH_{AB}^{mix} (kJ/mol), in the $Gd_xCoCrCuFeNi$ high-entropy alloys calculated by Miedema's approach [25].

Element (Melting point, Atomic radius)	Gd	Co	Cr	Fe	Cu	Ni
Gd (1313 °C, 180 pm)	-	−22	11	−1	−22	−31
Co (1495 °C, 125 pm)	-	-	−4	−1	6	0
Cr (1907 °C, 128 pm)	-	-	-	−1	12	−7
Fe (1538 °C, 126 pm)	-	-	-	-	13	−2
Cu (1084.6 °C, 128 pm)	-	-	-	-	-	4
Ni (1455 °C, 124 pm)	-	-	-	-	-	-

alloys, a small amount of white ID regions (about 15%) are identified as a Cu-rich FCC phase, which corresponds to the minor peak mentioned in the XRD analysis (Fig. 1). The ID regions are confirmed to be the Cu-rich HS phase in the $Gd_{0.1}$, $Gd_{0.2}$, and Gd_{03} alloys according to the XRD pattern shown in Fig. 1. Meanwhile, with increasing the Gd content, the volume fraction of the HS phase increases from 29.1% to 52.2% accordingly. The chemical compositions and the crystal structures of DR and ID regions of the alloy system are analyzed using the EDS and XRD, and the results are listed in Table 1. The EDS analysis indicates that Cu is depleted in the FCC matrix phase because of the positive mixing enthalpy of Cu-Cr, Cu-Co, Cu-Fe, and Cu-Ni (see Table 2), while Ni, Cu, and Gd are enriched in the HS phase because of the negative mixing enthalpy. In the present work, it is interesting to find that the addition of rare-earth element, Gd, can make the structure of the $Gd_xCoCrCuFeNi$ HEAs in the ID region change from the FCC phase to HS phase.

3.2. Nanoindentation tests

While the crystal structure and chemistry of the FCC and HS phases have been studied on the $Gd_xCoCrCuFeNi$ HEAs, the measurement of their mechanical properties is a challenging task due to their small size. The nanoindentation method has been used for the investigation of mechanical properties and deformation behavior in a small volume of materials, such as individual phases and the area around the grain boundary. Rehman et al. [25] have used the nanoindentation technology to study the mechanical properties of individual phases in nickel-based superalloys, and they found that the μ phase was harder and showed less work hardening than both the γ and the γ' phases. In the present work, nanoindentation measurements were performed to measure the nano-mechanical properties of individual phases.

There are two things that should be noticed during nanoindentation testing. For one thing, the maximum indentation load should be selected to keep the plastic zone size smaller than the size of individual phases. In the current work, the size of DR (> 50 μm) and ID (~ 10–60 μm) phases from the SEM images in Fig. 3 are enough to assure that the deformation is limited to the phase being indented under the maximum load of 5000 μN with the maximum penetration depth of ~ 190 nm (shown in Fig. 4(a)). For the other thing, the influence of varying the orientations of the indented phases on the nanoindentation tests should be considered. The measurement results of the present alloy system show that different orientations influence the nanoindentation results to a much lesser degree than the different crystal structure. And each mechanical property value represents an average of at least 20 measurements.

The typical *P-h* curves corresponding to the indentations into the FCC and HS phases of $Gd_{0.2}$ alloys are shown in Fig. 4(a). It is seen that the maximum penetration depth in the HS phase is ~ 105 nm, obviously shallower than that in the FCC phase (~ 190 nm), indicating that the HS phase is harder than the FCC phase. Both the nanohardness and elastic modulus of the FCC matrix, Cu-rich FCC, and HS phase of the $Gd_xCoCrCuFeNi$ HEAs are obtained according to the Oliver–Pharr method [26]. The nanohardness data in Fig. 4(b) showed that the FCC matrix and Cu-rich FCC phase have the same nanohardness value of ~ 3 GPa, and the value of the HS phase is ~ 10.5 GPa, which is almost three times that of the FCC phase. However, the fluctuation of elastic modulus is not so obvious, as shown in Fig. 4(c). The elastic-modulus value of the HS phase is ~ 190 GPa, which is just ~ 20 GPa higher than that of the FCC matrix and Cu-rich FCC (~ 170 GPa). There are three slip systems for the hexagonal structure metals, while the FCC metals have twelve slip systems. The more slip systems, the better plasticity. The HS phase has higher strength and lower plasticity than the FCC phase because the number of the independent slip system in the HS phase is lower. The present nanoindentation measurements directly verify that the HS phase ($CaCu_5$ type) containing the rare-earth element, Gd, is very strong than the FCC matrix and Cu-rich FCC phase. The first pop-in was the displacement burst in the *P-h* curves (Fig. 5(a)). It represented the elastic-to-plastic transition. The incipient plasticity of FCC and HS phases was characterized by measuring the first pop-in behavior. The dislocation nucleation on different phases will be discussed in detail in the next section.

3.3. Macro-mechanical properties

Room-temperature Vickers hardness and compression tests were performed to investigate effects of Gd additions on the macro-mechanical properties of the as-cast $Gd_xCoCrCuFeNi$ alloy system. Vickers hardness values of the $Gd_xCoCrCuFeNi$ HEAs are shown in Fig. 6. Due to no phase change, the Gd_0 and $Gd_{0.05}$ alloys have the same hardness values of 176 HV. A further increase of the Gd content results in a significant increase in hardness because of the formation of the HS phase. For example, the $Gd_{0.3}$ alloy has Vickers hardness of 293 HV. The increase in the volume fraction of the HS phase leads to the hardness

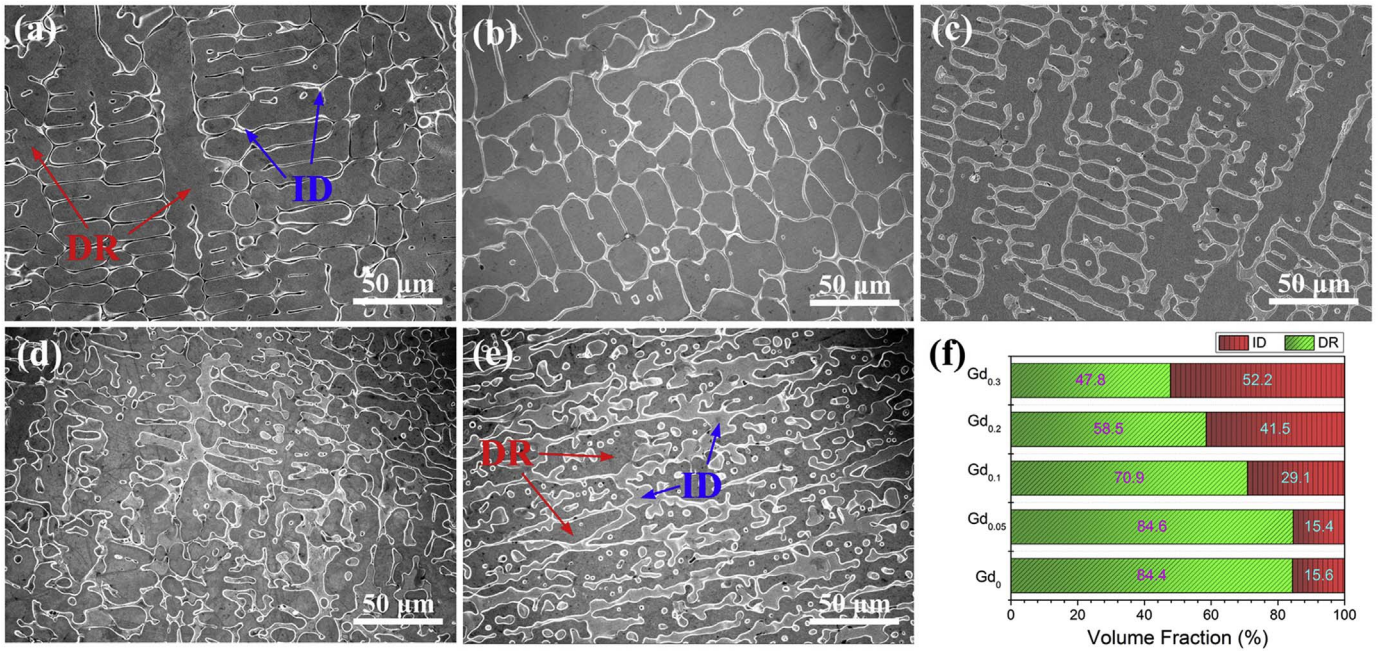

Fig. 3. SEM images of the as-cast $Gd_xCoCrCuFeNi$ alloys. (a) x = 0, (b) x = 0.05, (c) x = 0.1, (d) x = 0.2, and (e) x = 0.3. (f) The volume fraction of DR and ID regions.

increase from 223 HV ($Gd_{0.1}$ alloy) to 293 HV (the $Gd_{0.3}$ alloy).

Typical compressive engineering stress-strain curves for the current HEAs containing different amounts of the rare-earth element, Gd, are depicted in Fig. 7. The yield strength, σ_y, fracture strength, σ_f, and plastic strain, ε_p, as a function of the Gd content are summarized in Table 4. It is noted that the Gd content has an obvious effect on the compressive behavior of the alloy system. The Gd_0 alloy has low yield strength of 320 MPa, and a very pronounced work hardening stage after yielding. It is very ductile and is compressed to 60% height reduction without fracture. The $Gd_{0.05}$ alloy exhibits very similar behavior, although its yield strength value (300 MPa) is slightly lower than that of the Gd_0 alloy. A further increase in the Gd content results in substantial strengthening: the yield and fracture strengths of the $Gd_{0.1}$ alloy are 526 and 1410 MPa, respectively, but increase significantly to 1132 and 1836 MPa, respectively, in the $Gd_{0.3}$ alloy. In contrast, the plastic strain reduces appreciably from 22.9% in the $Gd_{0.1}$ alloy to 12.8% in the $Gd_{0.3}$ alloy. With the increase of the Gd content, the formation of the HS phase significantly enhances the hardness and strength of the HEAs due to the second-phase hardening from the HS phase.

Fracture surface and longitudinal-section microstructure of $Gd_xCoCrCuFeNi$ HEAs after compression test were shown in Fig. 8. The specimens of Gd_0 and $Gd_{0.05}$ alloys with excellent plasticity did not fracture after 60% compression strain but showed severe grain flow as shown in Fig. 8(a) and (b), respectively. The $Gd_{0.1}$ alloy did not have a portion departed from the fracture specimen after 30% compression strain. The longitudinal-section microstructure of the alloy was shown in Fig. 8(c). Some cracks initiation along the boundaries between ID and DR were observed. However, severe deformed grain along shear band indicated the alloy still had large plastic deformation ability. Fig. 8(d) and (e) presented the microstructure of the fracture surface of the $Gd_{0.2}$ alloy, which fractured after 23% compression strain. The presence of heavily deformed dimples indicated ductile fracture of the FCC matrix, while cleaved surfaces between the dimples indicate brittle fracture of the HS phase in this alloy. The brittle HS phase resulted in phase fragmentation and formation of fine particles (~ 1 μm), which can be clearly seen on the fracture surface in Fig. 8(e). The obvious river-like cleavage fracture (Fig. 8(f)) illustrated that a very brittle fracture feature of the $Gd_{0.3}$ alloy. Fig. 9 showed the TEM images of the longitudinal section of Gd_0 and $Gd_{0.1}$ alloys compressed by 30% and 15% at room temperature to give a further demonstration of the fracture mechanisms of the $Gd_xCoCrCuFeNi$ HEAs.

4. Discussion

4.1. Effect of Gd additions on the phase selection of $Gd_xCoCrCuFeNi$ alloys

For most HEAs, phase diagrams are still not well developed. So the phase-formation rules play an important role in the HEAs area. A couple of criteria have been proposed to predict and control the phase selection among solid solutions, intermetallic compounds, and the amorphous phase in HEAs. According to the thermodynamics and geometry effects, two effective criteria, $\Omega - \delta$ and $\Delta H_{mix} - \delta$, have been proposed by Yang [27] and Zhang [28]. These parameters are defined by the following equations [27,28]:

$$\Omega = \frac{T_m \Delta S_{mix}}{|\Delta H_{mix}|} \tag{1}$$

$$\Delta H_{mix} = \sum_{i=1, i\neq j}^{n} \Omega_{ij} c_i c_j \tag{2}$$

$$\delta = \sqrt{\sum_{i=1}^{n} c_i \left(1 - \frac{r_i}{\bar{r}}\right)^2} \tag{3}$$

where $T_m = \sum_{i=1}^{n} c_i (T_m)_i$, $(T_m)_i$ is the melting point of the ith constituent element (see Table 2); the entropy of mixing of an n-element alloy is $\Delta S_{mix} = -R \sum_{i=1}^{n} (c_i \ln c_i)$, R is the gas constant; c_i or c_j is the atomic percentage of the ith or jth component; $\Omega_{ij} = (4\Delta H_{AB}^{mix})$ is the regular solution-interaction parameter between the ith and jth elements, ΔH_{AB}^{mix} is the enthalpy of mixing the ith and jth components, calculated by the Miedema's approach [29]; $\bar{r} = \sum_{i=1}^{n} c_i r_i$ is the average atomic radius, and r_i is the atomic radius of the ith component (see Table 2). Experimental results indicate that solid solutions in HEAs are favored in the regions of $\Omega \geq 1.1$, $\delta \leq 6.6\%$ [27], and $-15 < \Delta H_{mix} < 5$ kJ/mol, $\delta \leq 6.6\%$ [28]. Beyond these regions, intermetallic compounds have a chance to occur. For the current Gd-containing alloys, the values of Ω, ΔH_{mix}, and δ are listed in Table 3. It can be seen in Table 3 that the Ω values of the alloy system range between 7.397 and 357.46, and ΔH_{mix} are between 3.2 and 0.071 kJ/mol. According to the above criteria, the values of Ω and ΔH_{mix} fall into the single solid solution region. The phase selection is determined by the value of δ ($\delta \leq 6.6\%$ for the

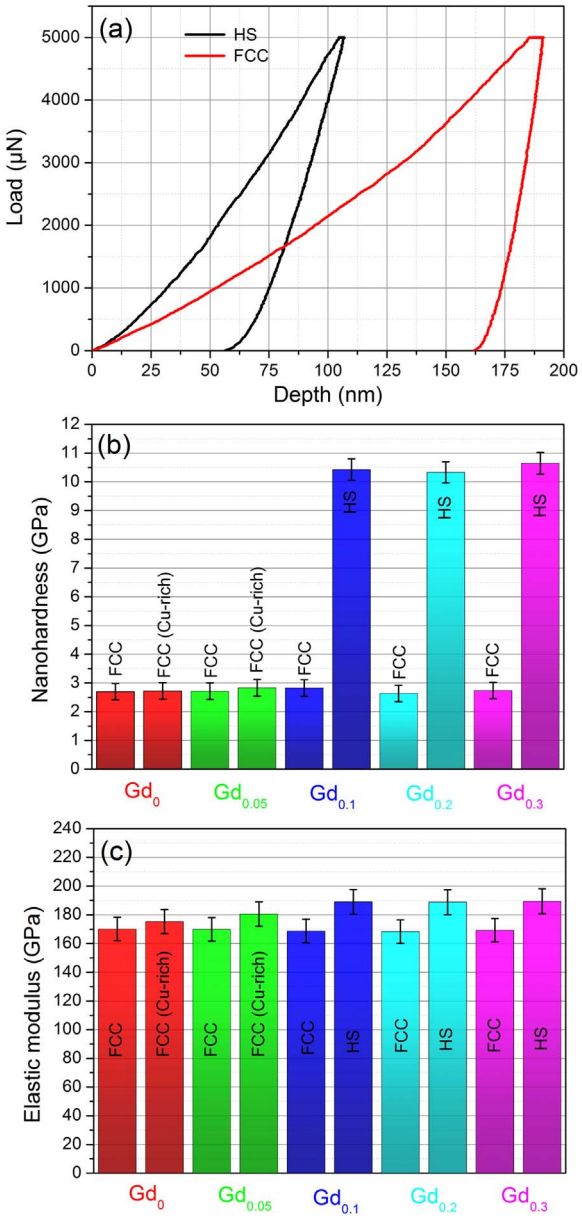

Fig. 4. (a) Typical load–displacement (*P-h*) curves for nanoindentation within the FCC matrix and HS phase of the $Gd_{0.2}$ alloy. (b) The average nanohardness on different phases of $Gd_xCoCrCuFeNi$ HEAs. (c) The average elastic modulus on different phases of $Gd_xCoCrCuFeNi$ HEAs.

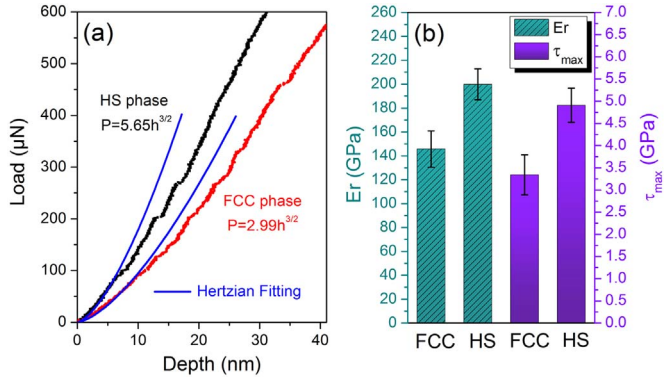

Fig. 5. (a) A typical first pop-in event at the beginning of the *P-h* curves of the FCC matrix and HS phase obtained with nanoindentation. (b) Average reduced modulus and the maximum shear stress on the FCC matrix and HS phase of $Gd_{0.2}$ alloy.

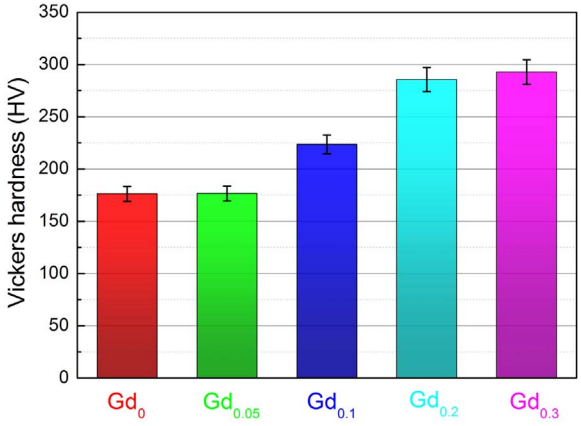

Fig. 6. Vickers hardness of the $Gd_xCoCrCuFeNi$ HEAs.

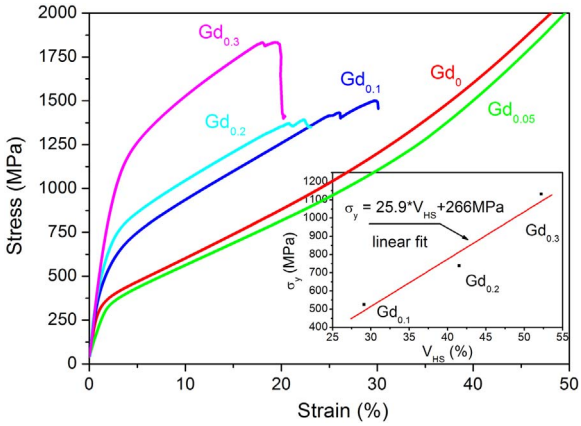

Fig. 7. Compressive engineering stress–strain curves of $Gd_xCoCrCuFeNi$ (x = 0, 0.05, 0.1, 0.2, and 0.3) alloys at room temperature, and the insert show the nearly linear relationship between σ_y and V_{HS} for $Gd_{0.1}$, $Gd_{0.2}$ and $Gd_{0.3}$ alloys.

Table 3
Calculated parameters ΔS_{mix}, ΔH_{mix}, Ω, δ, VEC, $\Delta\chi$, and Λ for the studied $Gd_xCoCrCuFeNi$ high-entropy alloys.

Alloys	ΔS_{mix}(J/mol/K)	ΔH_{mix}(kJ/mol)	Ω	δ(%)	VEC	$\Delta\chi$	Λ
Gd_0	13.381	3.2	7.397	1.267	8.8	0.0922	1.056
$Gd_{0.05}$	13.710	2.627	9.222	4.387	8.812	0.1113	0.313
$Gd_{0.1}$	13.921	2.076	11.838	5.992	8.823	0.1269	0.232
$Gd_{0.2}$	14.222	1.036	24.187	8.158	8.846	0.1521	0.174
$Gd_{0.3}$	14.432	0.071	357.46	9.694	8.868	0.1721	0.149

Table 4
Compression yield strength, σ_y, fracture strength, σ_f, and plastic strain, ε_p, of the $Gd_xCoCrCuFeNi$ high-entropy alloys.

Alloys	σ_y (MPa)	σ_f (MPa)	ε_p (%)
Gd_0	320	Not fractured	> 60
$Gd_{0.05}$	300	Not fractured	> 60
$Gd_{0.1}$	526	1410	22.9
$Gd_{0.2}$	739	1394	16.6
$Gd_{0.3}$	1132	1836	12.8

formation of solid solutions, $\delta > 6.6\%$ for the formation of intermetallic compounds). Apart from the $Gd_{0.1}$ alloy, all the values of other alloys can satisfy the two criteria judging from the Table 3. The $Gd_{0.1}$ alloy with $\delta = 5.992\%$ should have a single solid-solution phase. However, the HS phase even appeared in the $Gd_{0.1}$ alloy, and, thus, the two criteria fail to predict the phase selection in the current alloy system. Recent

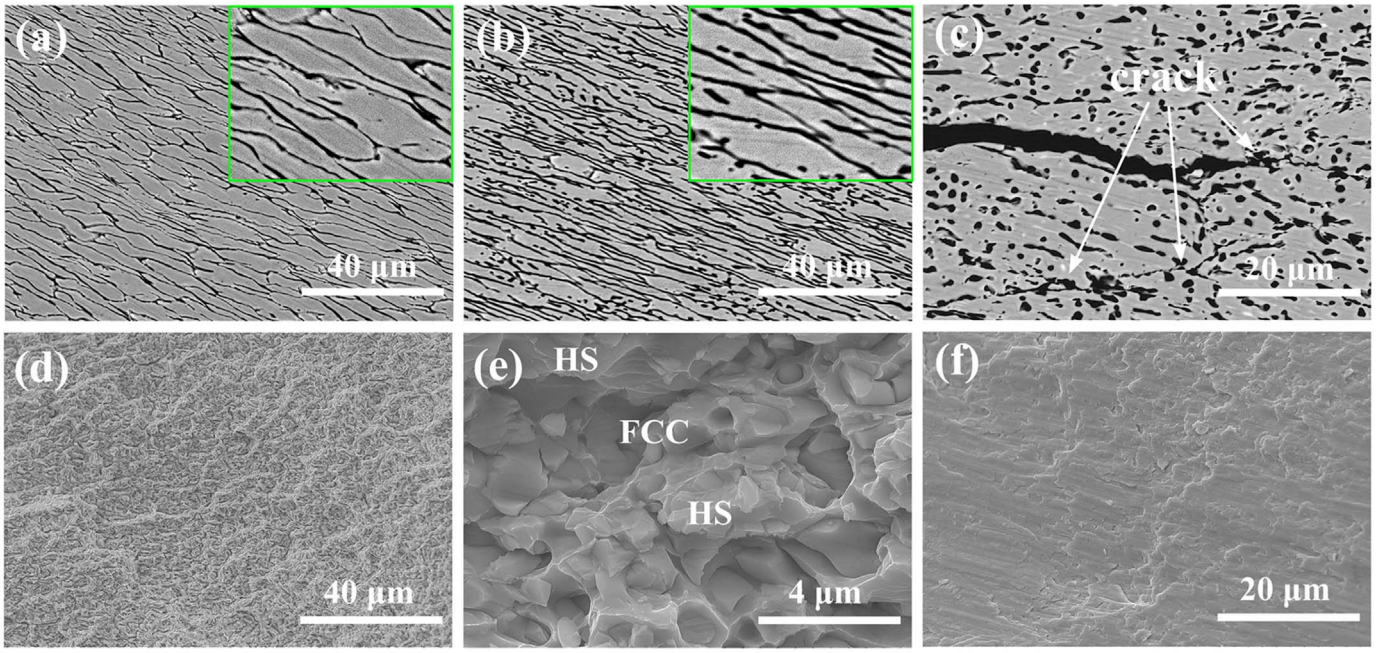

Fig. 8. The longitudinal-section SEM images of the Gd_0 alloy (a), the $Gd_{0.05}$ alloy (b), and the $Gd_{0.1}$ alloy (c) after compression deformation. (d) and (e) show the fracture surface morphology of the $Gd_{0.2}$ alloy. The microstructure of the fracture surface of the $Gd_{0.3}$ alloy is presented in (f).

article [30] pointed out that the Laves-phase formation in HEAs was governed by the difference between atomic sizes of the constitutive elements of the alloys, and the existing δ criterion ($\delta \leq 6.6\%$) did not allow predicting the Laves-phase formation. They attained the value of $\delta > 5\%$ for the Laves-phase formation from approximately 150 different HEAs, composed of either solid-solution or Laves phases. The HS phases with an AB_5 type are size-dependent compounds, i.e., in binary systems, their formation is observed when the atomic-size ratio, r_A/r_B, is in a range of 1.3 – 1.5 [23]. Meanwhile, the atomic-size-mismatch parameter of the HS phase containing alloys (5.992 – 9.694%, in Table 3) is significantly higher than that of the Laves-phase-containing alloys (5.295 – 7.787%) and BCC alloys (3.595 – 4.714%) [30]. Therefore, the value of $\delta > 5\%$ may be used to predict the formation of the HS phase of the present alloy system. As shown in Table 3, the values of δ for $Gd_{0.1}$, $Gd_{0.2}$, and $Gd_{0.3}$ alloys with the HS phase are noted to be in the range of 5.992 – 9.694%, falling within the region of $\delta > 5\%$.

The electro-negativity parameter, taking into account the similarity of the electronic structures of atoms of constitutive elements, was another important factor to predict the phase formation. The electro-negativity difference in a multicomponent alloy system was defined as $\Delta\chi$ [31] ($\Delta\chi = \sqrt{\sum_{i=1}^{n} c_i(\chi_i - \overline{\chi})^2}$, where χ_i is the Pauling electro-negativity for the ith element, and $\overline{\chi} = \sum_{i=1}^{n} c_i\chi_i$ is the average Pauling electro-negativity). The $\Delta\chi$ parameter ($\Delta\chi > 0.133$) has been used to predict the formation of the topologically close-packed (TCP) phase of HEAs [32]. However, the HS phase can be observed when $\Delta\chi > 0.12$ in the $Gd_xCoCrCuFeNi$ HEAs (see Table 3). In addition, other HEA-formation criteria, e.g., valence-electron concentration (VEC) [33] and geometrical parameter ($\Lambda = \Delta S_{mix}/\delta^2$) [34] were also examined for the current alloy system. The VEC values for the current alloy system are given in Table 3, and all of them fall into the FCC zone (VEC ≥ 8) according to the VEC criteria [33]. Thus, the VEC criterion is invalid for the current alloy system. Singh [34] has prescribed three ranges for the Λ-parameter for the formation of: (a) disordered solid solutions ($\Lambda > 0.96$), (b) a mixture involving compounds ($0.24 < \Lambda < 0.96$), and (c) (only) compound(s) ($\Lambda < 0.24$). The values of Λ listed in Table 3 suggested that the Λ-parameter criterion also failed to predict the phase formation in the current Gd-containing HEA system.

4.2. The incipient plasticity of FCC and HS phases

The nature of the nanohardness is the plastic flow, which is governed by interactions between moving dislocations and crystalline defects [35,36]. However, the first pop-in behavior represents the plastic yielding and is controlled by the dislocation nucleation when the shear-stresses approach theoretical limits (G/30 – G/5, where G is the shear modulus) underneath the indenter [36,37]. In order to further understand the effects of the crystal structure on the dislocation nucleation, nanoindentation experiments were performed on the FCC matrix and HS phase of the $Gd_{0.2}$ alloy to study the first pop-in behavior. The first pop-in is a sudden displacement burst in the loading segment of a *P-h* curve, which is associated with the onset of plasticity (an elastic-to-plastic transition). The deformation prior to the first pop-in is purely elastic deformation, and this elastic behavior could be described well by the Hertzian contact theory [38]:

$$P = \frac{4}{3}E_r R^{1/2} h^{3/2} \tag{4}$$

where P is the indentation load, h is indentation depth, R is the tip radius, and E_r is the reduced modulus given by $E_r = [(1 - \nu_i^2)/E_i + (1 - \nu_s^2)/E_s]^{-1}$, where ν_i (= 0.07) and E_i (= 1141 GPa) are the Poisson's ratio and Young's modulus of the indenter, ν_s and E_s are the Poisson's ratio and Young's modulus of the sample, respectively. The elastic segment of the first pop-in in the *P-h* curves of the FCC matrix and HS phase was well fitted by Eq. (4), as shown in Fig. 5(a). The average values of the reduced modulus were shown in Fig. 5(b).

According to the Hertzian contact theory, the maximum shear stress, τ_{max}, at the first pop-in load represents the critical shear yield strength for the onset of plasticity, and the τ_{max} occurs at a distance approximately half the contact radius directly below contact on the axis of symmetry. The magnitude of τ_{max} is given by [38]:

$$\tau_{\max} = 0.31 p_0 = 0.31\left(\frac{3}{2}p_m\right) = 0.31\left(\frac{6E_r^2}{\pi^3 R^2}P\right)^{\frac{1}{3}} \tag{5}$$

where p_0 and p_m are the maximum and mean pressures of the contact, respectively. As shown in Fig. 5(b), τ_{max} on the FCC matrix was

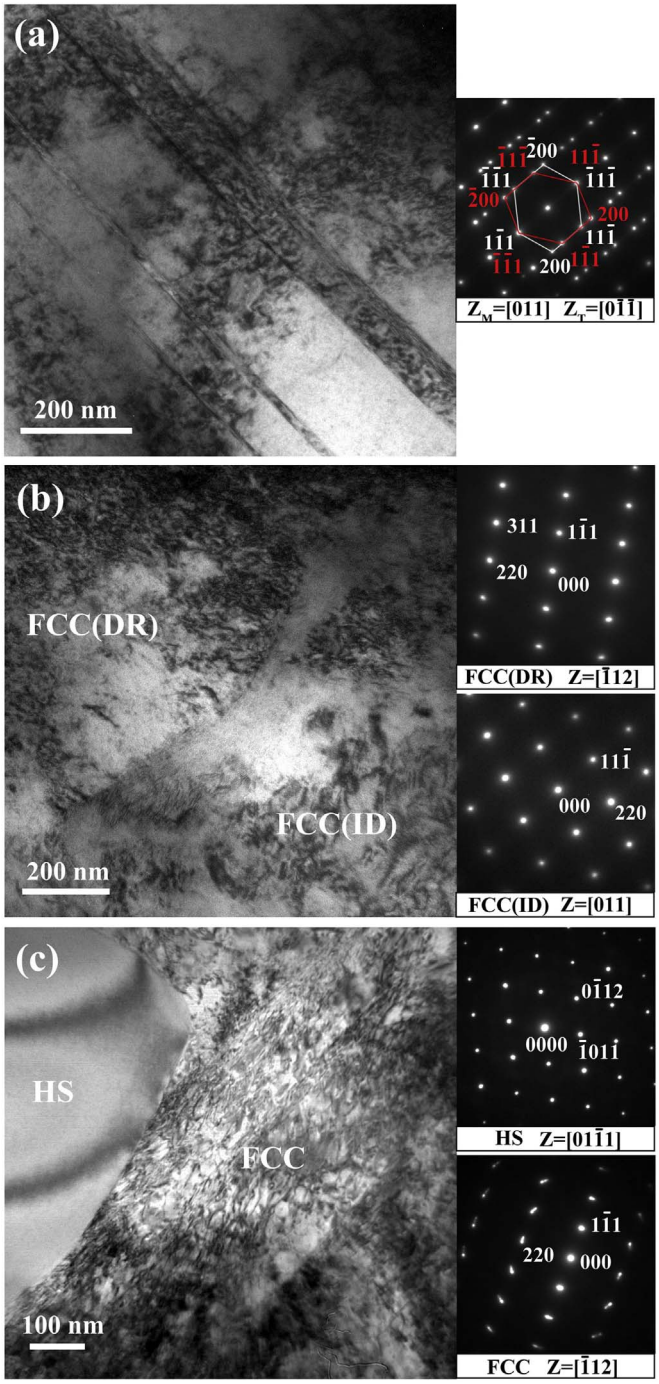

Fig. 9. TEM images and corresponding SAED patterns after 30% compression strain for Gd_0 alloy (a), (b) and after 15% compression strain for $Gd_{0.1}$ alloy (c).

calculated as ~ 3.3 GPa, which corresponded to $G_F/16$, where G_F was the shear modulus of the FCC matrix (~ 54 GPa, estimated from the Young's modulus and a Poisson's ratio of 0.3). The τ_{max} on the HS phase was ~ 5 GPa ($G_H/15$), where G_H (~ 75 GPa) was the shear modulus of the HS phase. The kind of dislocation nucleation underneath the indenter for different crystal structures has been identified. Ye and Wang et al. have calculated the activation energy for the nucleation of dislocations through measuring the first pop-in behavior and pointed out that the nucleation of full dislocations with the higher activation energy was favored in the BCC metals (e,g., Mo [39] or TiZrHfNb [40]), whereas the nucleation of partial dislocations with the lower activation energy was favored in FCC metals (e.g., Ni [39] or CoCrFeNiMn [40]). Catoor et al. [41] have concluded that the first pop-in behavior in all three orientations of the hexagonal close-packed (HCP) Mg single crystal was due to the homogeneous nucleation of full dislocations, and the shear stresses fall in the range of G/30 - G/14. The dislocation nucleation under the first pop-in can be described as a stress-assisted, thermally-activated process [42]. The energy barrier can be overcome when the applied stress exceeds τ_{max}. In comparison, we find that the dislocation nucleation for the FCC matrix can occur more easily with a lower τ_{max} than the HS phase with a higher τ_{max}. The reason may be that partial dislocations with the lower activation energy happen in the FCC matrix, and the full dislocations with a higher activation energy is favored in the HS phase. The large atomic-size difference for the rare-earth element, Gd, with the other constituent elements can result in the higher activation energy of dislocation nucleation.

4.3. Effect of Gd additions on macro-mechanical properties of $Gd_xCoCrCuFeNi$ alloys

As shown in Fig. 7, the Gd_0 and $Gd_{0.05}$ alloys containing two FCC phases exhibit excellent plasticity, but the $Gd_{0.1}$, $Gd_{0.2}$ and $Gd_{0.3}$ alloys possess high strength that increases with the Gd content because of the formation of the brittle HS phase. The improved mechanical properties primarily attribute to solid-solution strengthening and the second phase strengthening. For the single HEA, every atom is considered as the solute atom that occupies the crystal lattice sites randomly. The difference of the size and other properties of these solute atoms results in the severe lattice distortion. The interaction between the different atoms leads to the formation of a local elastic stress field that hinder the dislocation movements, resulting in an increase in strength. In the $Gd_xCoCrCuFeNi$ alloys, the hardness of FCC and HS phases show a slight increase with the increase of Gd content (Fig. 4). The second phase strengthening is the main strengthening mechanism of the current alloys. The increase of yield strength (or hardness) is proportional to the volume fraction of HS phase. To the first approximation, the strength of the alloys can be described by the simple rule-of-mixture [11] like the traditional composites: $\sigma_y = \sigma_{FCC}V_{FCC} + \sigma_{HS}V_{HS}$, where σ_{FCC} and σ_{HS} are the yield strength of the FCC and HS phases, V_{FCC} and V_{HS} are the volume fraction of the two phase, respectively, and $V_{FCC} + V_{HS} = 1$. So the equation can be converted to $\sigma_y = \sigma_{FCC} + (\sigma_{HS} - \sigma_{FCC})V_{HS}$. Consequently, the yield strength data measured from $Gd_{0.1}$, $Gd_{0.2}$ and $Gd_{0.3}$ alloys are plotted as a function of V_{HS} in the insert in Fig. 7. A good linear relationship was observed, indicating that the composite model can offer reasonable interpretation for the yield strength increment.

Next we will analyze the fracture mechanism of the GdxCoCrCuFeNi alloys. As shown in Fig. 4, the FCC matrix and Cu-rich FCC phase have almost the same hardness value, while the hardness of HS phase is three times FCC matrix phase, which means the yield strength of HS phase is higher than FCC phase. For the Gd_0 and $Gd_{0.05}$ alloys, the two FCC phases almost yield at the same time in the deformation process. The formation of a large amount of dislocation and the slip deformation will lead to the excellent plasticity (Fig. 8(a) and (b)). For the $Gd_{0.1}$, $Gd_{0.2}$ and $Gd_{0.3}$ alloys, the hard HS phase is still in the event of elastic deformation when the FCC matrix phase happens to yield in the initial stage of deformation. The hard and brittle HS phase can hinder the movement and expansion of dislocation. The HS phase will yield and produce cracks when further compression is deformed. Because of the small value of volume fraction of HS phase and the continuous distribution of FCC matrix phase, cracks do not expand soon, which leads to the combination of high strength and high plasticity in the $Gd_{0.1}$ and $Gd_{0.2}$ alloys. The HS phase will be the continuous phase when the volume fraction of HS phase increase to 52.2% in $Gd_{0.3}$ alloys. The crack propagation along the HS phase will happen soon, which results in brittle fracture of the sample (Fig. 8(f)). The crack propagation will lead to the HS phase fragmentation and the formation of fine particles (Fig. 8(e) and (f)) in the process of compression deformation.

In order to further reveal the fracture mechanism of $Gd_xCoCrCuFeNi$ HEAs, the TEM characterization of Gd_0 and $Gd_{0.1}$ alloys after different compression strain was carried out, as shown in Fig. 9. The TEM images and corresponding SAED patterns of ID and DR in Gd_0 alloy after 30% compression deformation were presented in Fig. 9(a) and (b). According to the SAED pattern in Fig. 9(a), strong reflections in the FCC matrix phase at zone axis orientation of [011] with twins on the {111} plane were present. The formation of twins was related to the relatively low stacking fault energy of HEAs [43,44]. A large amount of dislocations appeared in both FCC (DR) and FCC (ID) phase in Fig. 9(b). The accumulation of dislocations took place around the grain boundary between DR and ID. It should be noted that the movement of dislocation and the formation of twins contribute to the excellent plasticity of the Gd_0 alloy. The TEM bright field image with SAED patterns of $Gd_{0.1}$ alloy after 15% compression strain was shown in Fig. 9(c). It's obvious that a large number of dislocations distributed in FCC phase. The SAED pattern along the [1()12] FCC zone directions was elongated along the circumferential direction of the central spot, which meant deformation resulted in severe lattice distortion. However, few dislocations appeared in HS phase with high hardness and yield strength. The hard and brittle HS phase could enhance blocking the movement of dislocations. These suggested that there is no plastic deformation but direct brittle fracture for HS phase. Thus, the HS phase fragmentation resulted in the formation of fine particles rather than dimples.

5. Conclusions

In this study, the microstructure and mechanical behaviors of $Gd_xCoCrCuFeNi$ (x = 0, 0.05, 0.1, 0.2, and 0.3) HEAs were characterized. Alloying effects of the rare-earth element, Gd, on the phase formation and strength of these alloys were discussed. The nanomechanical properties on different phases were also discussed. Based on the obtained results and analyses, tentative conclusions can be drawn as follows.

(1) The additions of the Gd element into the CoCrCuFeNi HEA changed the original phase constitution and led to the formation of a new Cu-rich HS phase ($CaCu_5$ type) embedded in the FCC solid-solution matrix when the Gd content exceeded 0.05. Furthermore, the criteria ($\Omega - \delta$, $\Delta H_{mix} - \delta$, $\Delta\chi$, Λ, and VEC) cannot effectively predict the phases formation of the $Gd_xCoCrCuFeNi$ HEAs. However, the HS phase formation is observed when $\delta > 5\%$ and $\Delta\chi > 0.12$.
(2) Nanoindentation measurements were carried out on the FCC phases (a Cu-rich FCC and an FCC matrix) and HS phase. The HS phase has high nanohardness of 10.5 GPa, which is almost three times that of the FCC phase. The first pop-in behaviors of the incipient plasticity on the FCC matrix and HS phase indicated that the dislocation nucleation of the HS phase with the higher maximum shear stress of 5 GPa is harder than that of the FCC matrix with a lower maximum shear stress of 3.3 GPa.
(3) The minor Gd addition significantly increases the mechanical properties of the CoCrCuFeNi HEA. The hardness increases from 176 HV to 293 HV with the increase of the Gd content. The $Gd_{0.3}$ alloy has the yield strength of 1132 MPa, fracture strength of 1836 MPa, and plastic strain of 12.8%.

Acknowledgments

One of the authors (G. Li) acknowledges the Basic Research Project in the Hebei Province (Grant No. A2016203382), and the support from the National Science Foundation of China (Grant No. 11674274). P. F. Yu acknowledges the Research Program of the College Science & Technology of the Hebei Province (Grant No. QN2016167), and the National Natural Science Funds of China (Grant No. 51601166).

References

[1] J.W. Yeh, Recent progress in high-entropy alloys, Ann. Chim.-Sci. Mat. 31 (6) (2006) 633–648.
[2] Y. Zhang, T.T. Zuo, Z. Tang, M.C. Gao, K.A. Dahmen, P.K. Liaw, Z.P. Lu, Microstructures and properties of high-entropy alloys, Prog. Mater. Sci. 61 (2014) 1–93.
[3] Z. Tang, T. Yuan, C.W. Tsai, J.W. Yeh, C.D. Lundin, P.K. Liaw, Fatigue behavior of a wrought $Al_{0.5}CoCrCuFeNi$ two-phase high-entropy alloy, Acta Mater. 99 (2015) 247–258.
[4] M. Seifi, D. Li, Z. Yong, P.K. Liaw, J.J. Lewandowski, Fracture toughness and fatigue crack growth behavior of as-cast high-entropy alloys, JOM 67 (10) (2015) 2288–2295.
[5] Y.F. Ye, Q. Wang, J. Lu, C.T. Liu, Y. Yang, High-entropy alloy: challenges and prospects, Mater. Today 19 (6) (2016) 349–362.
[6] Y. Zhang, T.T. Zuo, Y.Q. Cheng, P.K. Liaw, High-entropy alloys with high saturation magnetization, electrical resistivity, and malleability, Sci. Rep.-UK 3 (2013).
[7] M.H. Chuang, M.H. Tsai, W.R. Wang, S.J. Lin, J.W. Yeh, Microstructure and wear behavior of $Al_xCo_{1.5}CrFeNi_{1.5}Ti_y$ high-entropy alloys, Acta Mater. 59 (16) (2011) 6308–6317.
[8] Y.L. Chou, Y.C. Wang, J.W. Yeh, H.C. Shih, Pitting corrosion of the high-entropy alloy $Co_{1.5}CrFeNi_{1.5}Ti_{0.5}Mo_{0.1}$ in chloride-containing sulphate solutions, Corros. Sci. 52 (10) (2010) 3481–3491.
[9] C. Lu, L. Niu, N. Chen, K. Jin, T. Yang, P. Xiu, Y. Zhang, F. Gao, H. Bei, S. Shi, Enhancing radiation tolerance by controlling defect mobility and migration pathways in multicomponent single-phase alloys, Nat. Commun. 7 (2016) 13564.
[10] W.R. Wang, W.L. Wang, S.C. Wang, Y.C. Tsai, C.H. Lai, J.W. Yeh, Effects of Al addition on the microstructure and mechanical property of $Al_xCoCrFeNi$ high-entropy alloys, Intermetallics 26 (7) (2012) 44–51.
[11] J.Y. He, W.H. Liu, H. Wang, Y. Wu, X.J. Liu, T.G. Nieh, Z.P. Lu, Effects of Al addition on structural evolution and tensile properties of the FeCoNiCrMn high-entropy alloy system, Acta Mater. 62 (1) (2014) 105–113.
[12] W.H. Liu, Z.P. Lu, J.Y. He, J.H. Luan, Z.J. Wang, B. Liu, Y. Liu, M.W. Chen, C.T. Liu, Ductile $CoCrFeNiMo_x$ high entropy alloys strengthened by hard intermetallic phases, Acta Mater. 116 (2016) 332–342.
[13] N.D. Stepanov, D.G. Shaysultanov, G.A. Salishchev, M.A. Tikhonovsky, E.E. Oleynik, A.S. Tortika, O.N. Senkov, Effect of V content on microstructure and mechanical properties of the $CoCrFeMnNiV_x$ high entropy alloys, J. Alloy Compd. 628 (2015) 170–185.
[14] F. He, Z.J. Wang, P. Cheng, Q. Wang, J.J. Li, Y.Y. Dang, J.C. Wang, C.T. Liu, Designing eutectic high entropy alloys of $CoCrFeNiNb_x$, J. Alloy Compd. 656 (2016) 284–289.
[15] Z.Q. Wang, X.R. Wang, H. Yue, G.T. Shi, S.H. Wang, Microstructure, thermodynamics and compressive properties of AlCoCrCuMn-x (x = Fe, Ti) high-entropy alloys, Mat. Sci. Eng. a-Struct. 627 (2015) 391–398.
[16] Y.J. Zhou, Y. Zhang, Y.L. Wang, G.L. Chen, Solid solution alloys of $AlCoCrFeNiTi_x$ with excellent room-temperature mechanical properties, Appl. Phys. Lett. 90 (18) (2007).
[17] K.H. Kong, C.K. Kang, W.T. Kim, D.H. Kim, Microstructural features of multicomponent $FeCoCrNiSi_x$ alloys, Appl. Microsc. 45 (1) (2015) 32–36.
[18] J. Chen, P.Y. Niu, Y.Z. Liu, Y.K. Lu, X.H. Wang, Y.L. Peng, J.N. Liu, Effect of Zr content on microstructure and mechanical properties of AlCoCrFeNi high entropy alloy, Mater. Des. 94 (2016) 39–44.
[19] S. Wang, H. Zhou, Y. Kang, The influence of rare earth elements on microstructures and properties of 6061 aluminum alloy vacuum-brazed joints, J. Alloy. Compd. 352 (1–2) (2003) 79–83.
[20] H. Mirzadeh, Quantification of the strengthening effect of rare earth elements during hot deformation of Mg-Gd-Y-Zr magnesium alloy, J. Mater. Res. Technol. 5 (1) (2016) 1–4.
[21] D.H. Xiao, J.N. Wang, D.Y. Ding, H.L. Yang, Effect of rare earth Ce addition on the microstructure and mechanical properties of an Al–Cu–Mg–Ag alloy, J. Alloy. Compd. 352 (1–2) (2003) 84–88.
[22] Q. Zhu, C. Fang, N. Li, L. Meng, W. Yu, Y. Wu, X. Zhang, Effects of rare-earth elements Gd and Nd on microstructure and mechanical properties of AZ80 magnesium alloy, Rare Metal. Mater. Eng. 42 (4) (2013) 771–775.
[23] L. Guenee, K. Yvon, Structure stability maps for intermetallic AB(5) compounds, J. Alloy Compd. 356 (2003) 114–119.
[24] M.L. Bhatia, Stability regime of the $CaCu_5$ structure, J. Alloy. Compd. 347 (1) (2002) 165–170.
[25] H.U. Rehman, K. Durst, S. Neumeier, A.B. Parsa, A. Kostka, G. Eggeler, M. Goken, Nanoindentation studies of the mechanical properties of the mu phase in a creep deformed Re containing nickel-based superalloy, Mat. Sci. Eng. a-Struct. 634 (2015) 202–208.
[26] W.C. Oliver, G.M. Pharr, An improved technique for determining hardness and elastic modulus using load and displacement sensing indentation experiments, J. Mater. Res. 7 (6) (1992) 1564–1583.
[27] X. Yang, Y. Zhang, Prediction of high-entropy stabilized solid-solution in multi-component alloys, Mater. Chem. Phys. 132 (2–3) (2012) 233–238.
[28] Y. Zhang, Y.J. Zhou, J.P. Lin, G.L. Chen, P.K. Liaw, Solid-solution phase formation rules for multi-component alloys, Adv. Eng. Mater. 10 (6) (2008) 534–538.
[29] A. Takeuchi, A. Inoue, Classification of bulk metallic glasses by atomic size difference, heat of mixing and period of constituent elements and its application to characterization of the main alloying element, Mater. Trans. 46 (12) (2006) 2817–2829.
[30] N. Yurchenko, N. Stepanov, G. Salishchev, Laves-phase formation criterion for high-

entropy alloys, Mater. Sci. Technol. (2016).
[31] S. Fang, X. Xiao, X. Lei, W. Li, Y. Dong, Relationship between the widths of supercooled liquid regions and bond parameters of Mg-based bulk metallic glasses, J. Non-Cryst. Solids 321 (1–2) (2003) 120–125.
[32] Y. Dong, Y. Lu, L. Jiang, T. Wang, T. Li, Effects of electro-negativity on the stability of topologically close-packed phase in high entropy alloys, Intermetallics 52 (4) (2014) 105–109.
[33] S. Guo, C. Ng, J. Lu, C.T. Liu, Effect of valence electron concentration on stability of fcc or bcc phase in high entropy alloys, J. Appl. Phys. 109 (10) (2011).
[34] A.K. Singh, N. Kumar, A. Dwivedi, A. Subramaniam, A geometrical parameter for the formation of disordered solid solutions in multi-component alloys, Intermetallics 53 (2014) 112–119.
[35] T. Ohmura, K. Tsuzaki, Plasticity initiation and subsequent deformation behavior in the vicinity of single grain boundary investigated through nanoindentation technique, J. Mater. Sci. 42 (5) (2007) 1728–1732.
[36] Y. Zhao, I.C. Choi, Y.J. Kim, J.I. Jang, On the nanomechanical characteristics of thermally-treated alloy 690: grain boundaries versus grain interior, J. Alloy Compd. 582 (2014) 141–145.
[37] S. Ogata, J. Li, N. Hirosaki, Y. Shibutani, S. Yip, Ideal shear strain of metals and ceramics, Phys. Rev. B Condens. Matter 70 (10) (2004) 2516–2528.
[38] K.L. Johnson, Contact mechanics, J. Tribol. 108 (4) (1985) 464.
[39] L. Wang, H. Bei, T.L. Li, Y.F. Gao, E.P. George, T.G. Nieh, Determining the activation energies and slip systems for dislocation nucleation in body-centered cubic Mo and face-centered cubic Ni single crystals, Scr. Mater. 65 (3) (2011) 179–182.
[40] Y.X. Ye, Z.P. Lu, T.G. Nieh, Dislocation nucleation during nanoindentation in a body-centered cubic TiZrHfNb high-entropy alloy, Scr. Mater. 130 (2017) 64–68.
[41] D. Catoor, Y.F. Gao, J. Geng, M.J.N.V. Prasad, E.G. Herbert, K.S. Kumar, G.M. Pharr, E.P. George, Incipient plasticity and deformation mechanisms in single-crystal Mg during spherical nanoindentation, Acta Mater. 61 (8) (2013) 2953–2965.
[42] J.K. Mason, A.C. Lund, C.A. Schuh, Determining the activation energy and volume for the onset of plasticity during nanoindentation, Phys. Rev. B Condens. Matter 73 (5) (2006) 054102.
[43] H. Zhang, Y.Z. He, Y. Pan, S. Guo, Thermally stable laser cladded CoCrCuFeNi high-entropy alloy coating with low stacking fault energy, J. Alloy Compd. 600 (2014) 210–214.
[44] A.J. Zaddach, C. Niu, C.C. Koch, D.L. Irving, Mechanical properties and stacking fault energies of NiFeCrCoMn high-entropy alloy, JOM 65 (12) (2013) 1780–1789.